



# Wall model for large-eddy simulation based on the lattice Boltzmann method



O. Malaspinas <sup>a,b,\*</sup>, P. Sagaut <sup>a</sup>

<sup>a</sup> Institut Jean le Rond d'Alembert, UMR 7190, Université Pierre et Marie Curie – Paris 6, 4 place Jussieu, case 162, F-75252, France

<sup>b</sup> Centre Universitaire d'Informatique, Université de Genève, 7, route de Drize, CH-1227, Switzerland

## ARTICLE INFO

### Article history:

Received 29 August 2013

Received in revised form 6 June 2014

Accepted 12 June 2014

Available online 17 June 2014

### Keywords:

Lattice Boltzmann method

Large-eddy simulation

Boundary layer

Wall modeling

Subgrid modeling

Turbulent plane channel

## ABSTRACT

An original wall-model for lattice Boltzmann based large-eddy simulation is presented. It relies on either an analytical profile for the velocity profile within the first off-wall cell or the solution of Turbulent Boundary Layer Equations. The latter are solved thanks to a meshless approach to obtain a user-friendly method. The proposed method is observed to be both robust and accurate, yielding very satisfactory results in plane channel flow up to  $Re_\tau = 20000$  on uniform grids with  $\Delta x^+ = \Delta y^+ = \Delta z^+ = 1000$ . The computed maximum error on skin friction is about 4% in most investigated cases on the coarsest grids (10 grid points across the half-channel height). It lies within 1–2% on finer grids with 20–60 uniformly distributed grid points in the channel half-height.

© 2014 Elsevier Inc. All rights reserved.

## 1. Introduction

Large-eddy simulation (LES) has become a powerful and useful unsteady simulation technique for turbulent flows, for both fundamental and applied research (see [38,15,40]). One among the main issues faced by LES is handling high-Reynolds wall-bounded flows. The very reason for that is that classical subgrid models used to parametrize unresolved scales are very simple models that cannot account for turbulence production, leading to the constraint that the computational grid resolution must be fine enough to capture turbulence producing events. In a turbulent boundary layer, that constraint yields drastic grid resolution requirements, the total number of grid points being proportional to  $O(Re^n)$  with  $n = 9/5$  (see [8,35,44]) or  $n = 13/7$  (in [10]), and such simulations are referred to as wall-resolved LES or quasi-DNS.

Some specific subgrid models must be used to alleviate this constraint, allowing for LES of high-Reynolds turbulent wall-bounded flows. The key idea is to increase the complexity of the subgrid model in the near-wall region in order to take into account the inner-layer physics. These dedicated subgrid models are referred to as wall models, yielding the wall-modeled LES approach. This approach allows for a drastic reduction in the number of required grid points, which is evaluated as  $O(Re^m)$  with  $m = 2/5$  (see [8,35,44]) or  $m = 1$  (see [10]). Such an approach was already investigated in the early times of LES research [11], and is still a very active research topic (see [35,38] for recent reviews). All wall models are based on a statistical description of flow features within the first grid cell at the wall, i.e. on a Reynolds-Averaged Navier–Stokes (RANS) approach inside the first cell of the LES simulation. Many different strategies have been proposed, ranging from enforcing an a priori mean velocity profile within the first cell to solving Turbulent Boundary Layer Equations (TBLE) (see [51,54,35,53]).

\* Corresponding author at: Institut Jean le Rond d'Alembert, UMR 7190, Université Pierre et Marie Curie – Paris 6, 4 place Jussieu, case 162, F-75252, France.

E-mail addresses: [malaspinas@lmm.jussieu.fr](mailto:malaspinas@lmm.jussieu.fr) (O. Malaspinas), [pierre.sagaut@upmc.fr](mailto:pierre.sagaut@upmc.fr) (P. Sagaut).

The latter approach can be interpreted as a particular case of hybrid RANS/LES coupling (see [49,50]). It is observed to be more flexible and more accurate than wall models directly based on an arbitrary mean velocity profile model, since it can account for pressure gradient, unsteadiness, convective effects and more complex physical mechanisms, such as temperature dynamics [3] or compressibility effects [5]. An interesting point is that it can be implemented in a meshless way (see [30]). Effects mentioned above are implicitly taken into account matching the flow at the edge of the first cell in a local and instantaneous way, leading to a good efficiency at predicting separation, as observed by Wang and Moin [52]. In the case of very strong effects within the first cells, these terms could be extrapolated from the first LES cell, allowing for a purely local treatment.

Wall-model efficiency is greatly dependent on the numerical implementation, since it provides the LES simulation with a new boundary condition at the wall in place of the classical no-slip boundary condition. Here, it is worth emphasizing that the vast majority of articles dealing with wall-modeled LES are based on cell-centered finite-volume methods for incompressible Navier–Stokes equations. Changes in the numerical methods, e.g. moving from cell-centered to cell-vertex methods, necessitate a deep and non-trivial revision of original implementation of the model to maintain both accuracy and numerical stability.

The present work deals with the extension of TBLE wall-models for LES based on lattice Boltzmann methods (LBM). These methods are now very popular for subsonic aerodynamics and aeroacoustics. A striking observation is that they are now the most used simulation tool for external unsteady aerodynamics and aeroacoustics in the automotive industry. A growing attention has been paid to LBM-based large-eddy simulation since the early 1990's (see [18,21,14,26]), leading to the definition of many closures strategies, ranging from extension of usual subgrid-viscosity models to more general Approximate Deconvolution Models [39,25]. But wall modeling for LBM-LES is still at its very early development stage, since only crude approaches have been implemented up to now, mostly based on the enforcement of a logarithmic mean velocity profile within the first cell. In the present paper, we address the extension of both velocity-profile-based and TBLE-based wall models to the lattice Boltzmann framework. Among the main differences between Navier–Stokes based wall-models and the LBM framework, one should notice that i) LBM describes a weakly compressible flow, involving a need for a boundary condition on density/pressure, ii) LBM unknowns are velocity distribution functions, not velocities, therefore skin friction cannot be directly utilized, and iii) most LBM methods rely on uniform grids, while Navier–Stokes LES is classically performed on stretched grids in the near-wall region to capture boundary-layer physics.

The paper is organized as follows. Section 2 displays a brief reminder about LBM fundamentals, including boundary condition definition and implementation. The key elements of LBM-based large-eddy simulation are then given in Section 3. Wall-modeling for LBM-LES is addressed in Section 4, in which an original wall-model for LBM-LES is proposed. The new model is assessed in Section 5, and conclusions are presented in Section 6.

## 2. A short introduction to the lattice Boltzmann method

In this section, we quickly reproduce the main steps for the construction of the lattice Boltzmann method. We do not intend to reproduce the computations in their integrality. For more informations and details the interested reader should refer to d'Humières et al. [13], Shan et al. [42], Succi [45], Aidun and Clausen [2], Malaspinas [24] among others.

### 2.1. The lattice Boltzmann scheme

The Boltzmann equation describes the time evolution of the velocity distribution function  $f(\mathbf{x}, \boldsymbol{\xi}, t)$  of finding a particle with velocity  $\boldsymbol{\xi}$  at position  $\mathbf{x}$  and at time  $t$ . The lattice Boltzmann scheme is a clever discretization of the continuous Boltzmann equation, where the collision operator is a relaxation of the distribution function  $f(\mathbf{x}, \boldsymbol{\xi}, t)$  towards a local equilibrium distribution.

Our starting point is the discretized (in velocity space) multiple-relaxation-time (MRT) equation (see d'Humières et al. [13] for example)

$$\partial_t f_i(\mathbf{x}, t) + \boldsymbol{\xi}_i \cdot \nabla f_i(\mathbf{x}, t) = -\Omega_{ij} (f_j(\mathbf{x}, t) - f_j^{(0)}(\mathbf{x}, t)) + F_i, \quad (1)$$

where summation is understood over repeated indexes,  $\Omega_{ij}$  is the multiple-relaxation-time operator,  $f_i(\mathbf{x}, t) \equiv f(\mathbf{x}, \boldsymbol{\xi}_i, t)$ ,  $f_i^{(0)}(\mathbf{x}, t) \equiv f^{(0)}(\mathbf{x}, \boldsymbol{\xi}_i, t)$ , and  $F_i$  is the forcing term. The velocity set  $\{\boldsymbol{\xi}_i\}_{i=0}^{q-1}$  is chosen such as fifth order polynomials can be integrated exactly by Gauss–Hermite quadrature. Such a quadrature is for instance given by the D3Q15, D3Q19 or D3Q27 lattice (three space dimensions, 15, 19, or 27 quadrature points in the velocity space, i.e. discrete velocities, see Shan et al. [42] for example). In this work only the D3Q19 quadrature is considered

$$\begin{aligned} \{\boldsymbol{\xi}_i\}_{i=0}^{18} = & \{(0, 0, 0), \\ & (-1, 0, 0), (0, -1, 0), (0, 0, -1), \\ & (-1, -1, 0), (-1, +1, 0), (-1, 0, -1), (-1, 0, +1), (0, -1, -1), (0, -1, +1), \\ & (+1, 0, 0), (0, +1, 0), (0, 0, +1), \\ & (+1, +1, 0), (+1, -1, 0), (+1, 0, +1), (+1, 0, -1), (0, +1, +1), (0, +1, -1)\}, \end{aligned}$$

and the weights  $w_i$  are given by

$$w_0 = 1/3, \quad w_{1,2,3,10,11,12} = 1/18, \quad w_{4,5,6,7,8,9,13,14,15,16,17,18} = 1/36.$$

The equilibrium distribution function  $f_i^{(0)}$  and forcing terms are given by

$$f_i^{(0)} = w_i \rho \left( 1 + \frac{\xi_i \cdot \mathbf{u}}{c_s^2} + \frac{1}{2c_s^4} \mathbf{Q}_i : \mathbf{u}\mathbf{u} \right), \quad (2)$$

$$F_i = \rho w_i \left( \frac{\xi_i - \mathbf{u}}{c_s^2} - \frac{(\xi_i \cdot \mathbf{u}) \xi_i}{c_s^4} \right) \cdot \mathbf{g}, \quad (3)$$

where  $\mathbf{Q}_i = \xi_i \xi_i - c_s^2 \mathbf{I}$  ( $\mathbf{I}$  being the identity matrix),  $c_s = 1/\sqrt{3}$  is the sound speed of the lattice,  $\rho$ ,  $\mathbf{u}$ , and  $\mathbf{g}$  are respectively the density, velocity and force fields. The density and velocity can be computed from the discretized distribution function  $f_i$  via

$$\rho = \sum_{i=0}^{q-1} f_i = \sum_{i=0}^{q-1} f_i^{(0)}, \quad (4)$$

$$\rho \mathbf{u} = \sum_{i=0}^{q-1} \xi_i f_i = \sum_{i=0}^{q-1} \xi_i f_i^{(0)}. \quad (5)$$

To these quantities we also add the stress tensor  $\mathbf{P}$  given by

$$\mathbf{P} = \sum_{i=0}^{q-1} \mathbf{c}_i \mathbf{c}_i f_i, \quad (6)$$

where  $\mathbf{c}_i \equiv \xi_i - \mathbf{u}$ . In the MRT framework a further assumption is made on  $\mathbf{\Omega}$  which is that it can be diagonalized with the transformation matrix  $\mathbf{M}$

$$\mathbf{A} = \mathbf{M} \mathbf{\Omega} \mathbf{M}^{-1}, \quad (7)$$

where  $\mathbf{A} = \text{diag}(\lambda_0, \dots, \lambda_{q-1})$  and  $\lambda_i$  are the relaxation frequencies of the model. If  $\lambda_i = \omega, \forall i$  then this model is equivalent with the popular BGK model (see Bhatnagar et al. [4]). The transformation matrix  $\mathbf{M}$  projects the populations into moment space (see Appendix A for a possible choice of  $\mathbf{M}$ ). Noting  $\mathbf{m}$  (respectively  $\mathbf{m}^{(0)}$ ) the moments vector (respectively equilibrium moments vector), and similarly  $\mathbf{f}$  (respectively  $\mathbf{f}^{(0)}$ ) the populations vector (respectively the equilibrium populations vector), one has

$$\mathbf{m} = \mathbf{M} \mathbf{f}, \quad \mathbf{m}^{(0)} = \mathbf{M} \mathbf{f}^{(0)}. \quad (8)$$

With the definitions of Appendix A one has that

$$m_0^{(0)} = m_0 = \rho, \quad m_1^{(0)} = \rho(-11 + 19u_x^2 + 19u_y^2 + 19u_z^2), \quad (9)$$

$$m_2^{(0)} = \frac{11}{2} \rho(3 - u_x^2 - u_y^2 - u_z^2), \quad m_3^{(0)} = m_3 = \rho u_x, \quad (10)$$

$$m_4^{(0)} = -\frac{2}{3} \rho u_x, \quad m_5^{(0)} = m_5 = \rho u_y, \quad (11)$$

$$m_6^{(0)} = -\frac{2}{3} \rho u_y, \quad m_7^{(0)} = m_7 = \rho u_z, \quad (12)$$

$$m_8^{(0)} = -\frac{2}{3} \rho u_z, \quad m_9^{(0)} = 2\rho u_x^2 - \rho u_y^2 - \rho u_z^2, \quad (13)$$

$$m_{10}^{(0)} = -\rho u_x^2 + \frac{1}{2} \rho u_y^2 + \frac{1}{2} \rho u_z^2, \quad m_{11}^{(0)} = \rho u_y^2 - \rho u_z^2, \quad (14)$$

$$m_{12}^{(0)} = -\frac{1}{2} \rho u_y^2 + \frac{1}{2} \rho u_z^2, \quad m_{13}^{(0)} = \rho u_x u_y, \quad (15)$$

$$m_{14}^{(0)} = \rho u_z u_y, \quad m_{15}^{(0)} = \rho u_x u_z, \quad (16)$$

$$m_{16}^{(0)} = m_{17}^{(0)} = m_{18}^{(0)} = 0. \quad (17)$$

Noting the matrix  $\mathcal{E}_{\alpha i} \equiv \xi_{\alpha i}$ , with alpha the spatial indexes, and with the above definitions one has the following discretized in velocity space MRT equation

$$\partial_t \mathbf{f} + (\mathcal{E} \cdot \nabla) \mathbf{f} = -\mathbf{M}^{-1} \mathbf{A} (\mathbf{m} - \mathbf{m}^{(0)}) + \mathbf{F}, \quad (18)$$

where  $\mathbf{F}$  is the forcing term vector. Defining  $\mathbf{m}^{\text{eq}}$  as

$$\mathbf{m}^{\text{eq}} = \mathbf{m}^{(0)} + \Lambda^{-1} \mathbf{M} \mathbf{F}, \quad (19)$$

one can rewrite Eq. (18) as

$$\partial_t \mathbf{f} + (\boldsymbol{\Xi} \cdot \nabla) \mathbf{f} = -\mathbf{M}^{-1} \Lambda (\mathbf{m} - \mathbf{m}^{\text{eq}}). \quad (20)$$

Before proceeding with the discretization of this equation, this scheme is known to asymptotically lead to the weakly compressible Navier–Stokes equations through a Chapman–Enskog expansion (see Chapman and Cowling [9], d’Humières [12], d’Humières et al. [13] for details). This expansion is based on the assumption that the distribution function is decomposed into its equilibrium part  $f_i^{(0)}$  and a small perturbation  $f_i^{(1)}$  (which is proportional to the Knudsen number)

$$f_i = f_i^{(0)} + f_i^{(1)}, \quad f_i^{(1)} \ll f_i^{(0)}. \quad (21)$$

We also assume that  $\mathbf{g} \cong \mathbf{g}^{(1)}$ , with  $\mathbf{g}^{(1)} \sim \|\mathbf{f}^{(1)}\|$ , and therefore

$$\mathbf{F} \cong \mathbf{F}^{(1)} = \rho w_i \left( \frac{\xi_i - \mathbf{u}}{c_s^2} - \frac{(\xi_i \cdot \mathbf{u}) \xi_i}{c_s^4} \right) \cdot \mathbf{g}^{(1)}. \quad (22)$$

From these definitions and the mass and momentum conservation constraints one has that

$$\sum_i f_i^{(1)} = \sum_i \xi_i f_i^{(1)} = 0, \quad (23)$$

and that the stress tensor  $\mathbf{P}$  can also be accordingly decomposed as

$$\mathbf{P} = \mathbf{P}^{(0)} + \mathbf{P}^{(1)} = c_s^2 \rho \mathbf{I} + \mathbf{P}^{(1)}. \quad (24)$$

Replacing Eq. (21) in Eq. (20) and keeping only the leading order in the equation one finds

$$\partial_t \mathbf{f}^{(0)} + (\boldsymbol{\Xi} \cdot \nabla) \mathbf{f}^{(0)} = -\mathbf{M}^{-1} \Lambda \mathbf{m}^{(1)} + \mathbf{F}^{(1)}, \quad (25)$$

where  $\mathbf{m}^{(1)} = \mathbf{M} \mathbf{f}^{(1)}$ . Taking the zeroth order moment of this equation one finds the mass conservation equation

$$\partial_t \rho + \nabla \cdot (\rho \mathbf{u}) = 0. \quad (26)$$

Taking the first moment of Eq. (25) one obtains

$$\partial_t (\rho \mathbf{u}) + \nabla \cdot (\rho \mathbf{u} \mathbf{u}) = -\nabla p - \nabla \cdot \mathbf{P}^{(1)} + \rho \mathbf{g}, \quad (27)$$

with the pressure  $p = c_s^2 \rho$ . The second order moment of Eq. (25) finally gives us the constitutive equation for the deviatoric stress

$$\mathbf{P}^{(1)} = -2\rho \nu \mathbf{S}, \quad (28)$$

where  $\nu = c_s^2 / \lambda_\nu$ , and  $\lambda_\nu = \lambda_{9,11,13,14,15}$ . Furthermore the non-equilibrium part of the distribution function  $f_i^{(1)}$  can be approximated by

$$f_i^{(1)} = \frac{w_i}{2c_s^4} \mathbf{Q}_i : \mathbf{P}^{(1)} = -\frac{w_i \rho}{c_s^2 \lambda_\nu} \mathbf{Q}_i : \mathbf{S}. \quad (29)$$

While the  $\lambda_{0,3,5,7}$  are parameters that are not affecting the dynamics of the flow. The remaining parameters are free and can be defined through a linear stability analysis (see [13,37,28,46,47]). The free parameters used in this paper are detailed in Appendix A. We now focus our attention on the time–space discretization of Eq. (20).

Rewriting the equation as

$$\frac{d}{dt} \mathbf{f} = -\mathbf{M}^{-1} \Lambda (\mathbf{m} - \mathbf{m}^{\text{eq}}) \quad (30)$$

and integrating it along characteristics with the trapezoidal rule, one gets ( $\delta t = 1$ )

$$\mathbf{f}^+ - \mathbf{f} = -\frac{1}{2} \mathbf{M}^{-1} \Lambda (\mathbf{m}^+ - \mathbf{m}^{(0)+} + \mathbf{m} - \mathbf{m}^{(0)}), \quad (31)$$

where the superscript “+” stands for the evaluation at  $t + 1$  and  $\mathbf{x} + \boldsymbol{\xi}_i$ .

Imposing the following change of variables and defining  $\hat{\Lambda} \equiv \Lambda + \mathbf{I}/2$

$$\hat{\mathbf{f}} = \mathbf{f} + \frac{\mathbf{M}^{-1} \Lambda}{2} (\mathbf{m} - \mathbf{m}^{\text{eq}}), \quad (32)$$

one obtains the MRT lattice Boltzmann scheme

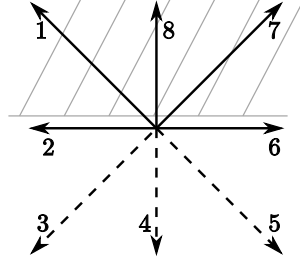


Fig. 1. A boundary node for the D2Q9 lattice. The dashed arrows represent the unknown populations.

$$\hat{\mathbf{f}}^+ = \hat{\mathbf{f}} - \mathbf{M}^{-1} \hat{\mathbf{\Lambda}} (\hat{\mathbf{m}} - \mathbf{m}^{\text{eq}}), \quad (33)$$

which can also be rewritten as

$$\hat{\mathbf{f}}^+ = \hat{\mathbf{f}} - \mathbf{M}^{-1} \hat{\mathbf{\Lambda}} (\hat{\mathbf{m}} - \mathbf{m}^{(0)}) + \left( \mathbf{I} - \frac{\hat{\mathbf{\Lambda}}}{2} \right) \mathbf{F}. \quad (34)$$

In an actual implementation the “hatted” populations are the ones that are used.

In order to compute the physical macroscopic quantities from  $\hat{\mathbf{f}}$  one uses Eq. (32) and it is straightforward to find that

$$\rho = \hat{\rho}, \quad (35)$$

$$\mathbf{u} = \hat{\mathbf{u}} + \frac{\mathbf{g}}{2}, \quad (36)$$

$$\mathbf{P}^{(1)} = \hat{\mathbf{P}}^{(1)} \left( 1 - \frac{\lambda_v}{2} \right) - \frac{1}{4c_s^4} \mathbf{g} \mathbf{g} \cong \hat{\mathbf{P}}^{(1)} \left( 1 - \frac{\lambda_v}{2} \right), \quad (37)$$

where in the last equality we used that  $\mathbf{g} \sim Kn$  and therefore  $\mathbf{g} \mathbf{g}$  is negligible. Furthermore the non-equilibrium part of the distribution function  $f_i^{(1)}$  can be approximated by

$$\hat{f}_i^{(1)} = \hat{f}_i - f_i^{(0)}(\hat{\rho}, \hat{\mathbf{u}}) = \frac{w_i}{2c_s^4} \mathbf{Q}_i : \hat{\mathbf{P}}^{(1)} = -\frac{w_i \rho}{c_s^2 \lambda_v} \mathbf{Q}_i : \mathbf{S}. \quad (38)$$

## 2.2. Boundary conditions for the lattice Boltzmann method

In this subsection we briefly present the boundary condition approach used in this paper. For more informations on boundary conditions in the lattice Boltzmann method the interested reader is referred to Bouzidi et al. [6], Guo and Zheng [17], Ginzburg and d’Humières [16], Latt et al. [23], Malaspinas et al. [27]. Here we only concentrate on Dirichlet boundary conditions, where the velocity is imposed. This discussion is valid for flat walls, but can be extended to more complicated geometries (see discussion at the end of this subsection).

From the algorithmic point of view the LBM scheme is decomposed in two steps:

### 1. The collision step

$$\hat{\mathbf{f}}^{\text{out}} = \hat{\mathbf{f}} - \mathbf{M}^{-1} \hat{\mathbf{\Lambda}} (\hat{\mathbf{m}} - \mathbf{m}^{(0)}) + \left( \mathbf{I} - \frac{\hat{\mathbf{\Lambda}}}{2} \right) \mathbf{F}. \quad (39)$$

### 2. The propagation/streaming step

$$\hat{f}_i(\mathbf{x} + \boldsymbol{\xi}_i, t + 1) = \hat{f}_i^{\text{out}}(\mathbf{x}, t). \quad (40)$$

Therefore on a boundary node there are populations that are unknown before the collision since they are streamed “from outside” the computational domain as depicted on Fig. 1 (for simplicity this example is done in 2D). Thus they have to be computed in an ad hoc manner. To this end there exist two main different approaches for the implementation of boundary conditions: those based on “bounce-back” approaches or those based on a reconstruction of populations with the help of their Chapman–Enskog expansion. In this paper we only use the latter.

The main idea is to reconstruct all the populations of the boundary node according to Eq. (38)

$$\hat{f}_i = f_i^{(0)}(\rho_{\text{bc}}, \hat{\mathbf{u}}_{\text{bc}}) + f_i^{(1)}(\hat{\mathbf{P}}_{\text{bc}}^{(1)}), \quad (41)$$

where  $\rho_{\text{bc}}$ ,  $\hat{\mathbf{u}}_{\text{bc}}$  and  $\hat{\mathbf{P}}_{\text{bc}}^{(1)}$  are the values of  $\hat{\rho}$ ,  $\hat{\mathbf{u}}$  and  $\hat{\mathbf{P}}^{(1)}$  on the boundary node.

The values of the velocity will be imposed in the following. The quantities that must be evaluated are the density and the stress. The density is computed following the method presented in Zou and He [48],

$$\rho_{bc} = \frac{1}{1 + \hat{u}_{bc}^\perp} (2\rho_+ + \rho_0), \quad (42)$$

where  $\hat{u}_{bc}^\perp = \hat{\mathbf{u}}_{bc} \cdot \mathbf{n}$  is the boundary velocity projected onto the boundary outward normal unit vector  $\mathbf{n}$ . The quantities  $\rho_0$  and  $\rho_+$  are defined as

$$\rho_0 = \sum_{i \in \{i | \xi_i \cdot \mathbf{n} = 0\}} \hat{f}_i, \quad (43)$$

$$\rho_+ = \sum_{i \in \{i | \xi_i \cdot \mathbf{n} > 0\}} \hat{f}_i. \quad (44)$$

This is illustrated in Fig. 1, in which  $\xi_i \cdot \mathbf{n} = 0$  for  $i = 2, 6, 9$ ,  $\xi_i \cdot \mathbf{n} < 0$  for  $i = 3, 4, 5$  and  $\xi_i \cdot \mathbf{n} > 0$  for  $i = 1, 7, 8$ . The off-equilibrium populations  $\hat{f}_i^{(1)}$  are proportional to the stress at the leading order and are given by Eq. (38)

$$\hat{f}_i^{(1)} = \frac{w_i}{2c_s^4} \mathbf{Q}_i : \hat{\mathbf{P}}^{(1)}.$$

Since  $\mathbf{Q}_i = \mathbf{Q}_{\text{opp}(i)}$  (where  $\text{opp}(i)$  labels the direction opposite to the direction pointed by  $\xi_i$ ) one can impose that

$$\hat{f}_i^{(1)} = \hat{f}_{\text{opp}(i)}^{(1)}, \quad \forall i | \xi_i \cdot \mathbf{n} < 0. \quad (45)$$

Then

$$\hat{\mathbf{P}}^{(1)} = \sum_i \mathbf{Q}_i \hat{f}_i^{(1)} \quad (46)$$

and  $\hat{f}_i$  can be reconstructed according to Eq. (41).

A possible straightforward (but not easy) approach to extend the proposed strategy to curved boundaries would be to use the method proposed in [17]. There in general a no-slip velocity must be imposed on regions that are lying in-between lattice nodes. This is done by interpolating the velocity (which is achieved by imposing the no-slip condition on “off-lattice” points), and by extrapolating the density and deviatoric stress (Eqs. (42) and (45) cannot be used anymore). Then the populations are reconstructed with Eq. (41). In what follows (see Subsection 4.2) the velocity that must be imposed on lattice nodes does not need to be interpolated, because it is assumed to have a prescribed shape and is known on all nodes close to the actual boundary.

### 3. Lattice Boltzmann method based large-eddy simulation: a brief reminder

In this section we reproduce the main results for large eddy simulations techniques using the lattice Boltzmann method. The emphasis is put on subgrid-viscosity closures. For more details the interested reader should refer to Hou et al. [18], Krafczyk et al. [21], Premnath et al. [36], Malaspinas and Sagaut [26] among others.

The LES model used in the bulk of the simulation is a static Smagorinsky model [43], where the non-resolved scales are modeled through an eddy viscosity and where the molecular viscosity  $\nu$  is replaced by the efficient viscosity  $\nu_{\text{eff}}$

$$\nu_{\text{eff}} = \nu + \nu_t, \quad \nu_t = (C\Delta)^2 \sqrt{2\bar{S}_{\alpha\beta}\bar{S}_{\alpha\beta}}, \quad (47)$$

where  $C$  is the Smagorinsky constant and  $\Delta = (\delta x \delta y \delta z)^{1/3}$  the filter width.

Recalling Eq. (34)

$$\hat{\mathbf{f}}^+ = \hat{\mathbf{f}} - \mathbf{M}^{-1} \hat{\mathbf{A}} (\hat{\mathbf{m}} - \mathbf{m}^{(0)}) + \left( \mathbf{I} - \frac{\hat{\mathbf{A}}}{2} \right) \mathbf{F},$$

in order to include an eddy viscosity model one only needs to replace the relaxation frequency  $\hat{\lambda}_\nu$  (contained in  $\hat{\mathbf{A}}$ ), by an efficient relaxation frequency  $\hat{\lambda}_{\nu, \text{eff}}$ , which amounts to have an efficient relaxation frequency  $\hat{\lambda}_{\nu, \text{eff}}$  in Eq. (34)

$$\hat{\lambda}_{\nu, \text{eff}} = (1/\hat{\lambda}_\nu + 1/\lambda_{\nu, t})^{-1}, \quad \lambda_{\nu, t} = \frac{c_s^2}{C^2} (2\bar{S}_{\alpha\beta}\bar{S}_{\alpha\beta})^{-1/2}. \quad (48)$$

The filtered strain rate can be computed either through finite difference or locally. Here we compute it locally through the following formula (see Malaspinas and Sagaut [26])

$$\bar{S}_{\alpha\beta} = \left( \frac{-\rho c_s^2 / \hat{\lambda}_\nu + \sqrt{(\rho c_s^2 / \hat{\lambda}_\nu)^2 + 2\rho c_s^4 C^4 \sqrt{2\hat{P}_{\alpha\beta}^{(1)} \hat{P}_{\alpha\beta}^{(1)}}}}{2\rho c_s^4 C^4 \sqrt{2\hat{P}_{\alpha\beta}^{(1)} \hat{P}_{\alpha\beta}^{(1)}}} \right) \hat{P}_{\alpha\beta}^{(1)}. \quad (49)$$

It is worth noting that the linear sum  $\nu_{\text{eff}} = \nu + \nu_t$  can be replaced by the harmonic mean  $\nu_{\text{eff}} = \sqrt{\nu^2 + \nu_t^2}$  to obtain an inertial-consistent subgrid viscosity model with an improved capture of finite-Reynolds number effects [14].

#### 4. Lattice Boltzmann method for boundary-layer modeling

##### 4.1. Turbulent boundary layer equations in the Navier–Stokes framework

In this subsection, we intend to quickly remind the reader the basic equations used for the modeling of turbulent boundary layer in the Navier–Stokes framework. For more informations see Schlichting and Gersten [41] for example.

In the Navier–Stokes framework the RANS equations can be simplified for the turbulent boundary layer (TBL) model thanks to the thin layer approximation. Assuming the mean flow direction to be in the  $x$  direction and the normal to the wall in the  $y$  direction, one obtains

$$\partial_y \langle p \rangle = 0, \quad (50)$$

$$\partial_t \langle \rho \rangle + \partial_x (\langle \rho \rangle \tilde{u}_x) + \partial_y (\langle \rho \rangle \tilde{u}_y) = 0, \quad (51)$$

$$\langle \rho \rangle (\partial_t \tilde{u}_x + \tilde{u}_x \partial_x \tilde{u}_x + \tilde{u}_y \partial_y \tilde{u}_x) = -\partial_x \langle p \rangle + \partial_y [(\mu + \mu_t) \partial_y \tilde{u}_x], \quad (52)$$

where  $\mu_t$  is the turbulent viscosity and where we defined  $\langle \phi \rangle$  the ensemble average of a quantity  $\phi$  and using Favre's density weighted average

$$\tilde{\phi} = \frac{\langle \rho \phi \rangle}{\langle \rho \rangle}. \quad (53)$$

Now assuming that the mean flow is parallel and statistically steady, one has

$$\partial_t \tilde{u}_x = \partial_x \tilde{u}_x = \tilde{u}_y = 0, \quad (54)$$

and the TBL equations (Eqs. (50)–(52)) simplify as

$$\partial_y \langle p \rangle = 0, \quad (55)$$

$$\partial_y [(\mu + \mu_t) \partial_y \tilde{u}_x] - \partial_x \langle p \rangle = 0. \quad (56)$$

A classical form of the eddy viscosity is

$$\mu_t = \langle \rho \rangle [\kappa y V_{A^+} (y^+)]^2 |\partial_y \tilde{u}_x|, \quad (57)$$

where  $\kappa$  is a constant (here it is chosen as  $\kappa = 0.384$  and its value is usually chosen between 0.37 and 0.41, see Nagib and Chauhan [33]), and  $V_{A^+}$  the Van Driest damping function

$$V_{A^+} (y^+) = 1 - \exp(-y^+ / A^+), \quad (58)$$

with  $A^+ = 26$  the van Driest parameter, and  $y^+ = y \sqrt{\tau_w / \langle \rho \rangle} / \nu$  is the position non-dimensionalized with respect to the wall friction  $\tau_w$ . The one dimensional equation (56) can be integrated numerically using a Gauss–Legendre quadrature (see Bocquet et al. [5] for a complete description of the algorithm used). It is worth noting that the parallel flow assumption is exact in internal flows such as the plane channel flow, while it is only a first-order approximation in quasi-parallel flows like spatially developing flat plate boundary layer. Previous authors [51,54,52,53,5] reported a very good accuracy for quasi-parallel flows and also in some separated flows, in which the quasi-parallel assumption does not hold. In the latter case, accuracy is recovered using medium size cells at the wall to minimize the wall-normal effects within the first cell.

There exist also quasi-analytical models that give the velocity profile inside the boundary layer (see among others Musker [32], Monkewitz et al. [31]). In this paper we will use the one proposed by Musker

$$\begin{aligned} \tilde{u}(y^+) = u_\tau \left[ 5.424 \arctan(0.119760479041916168 y^+ - 0.488023952095808383) \right. \\ \left. + 0.434 \log \left( \frac{(y^+ + 10.6)^{9.6}}{(y^{+2} - 8.15 y^+ + 86.0)^2} \right) - 3.50727901936264842 \right], \end{aligned} \quad (59)$$

with the friction velocity  $u_\tau$  defined as

$$u_\tau = \sqrt{\tau_w / \langle \rho \rangle}. \quad (60)$$

##### 4.2. Implementation of the TBL boundary condition on a flat wall

For the sake of clarity and simplicity we now detail how to implement the TBL boundary condition on a flat wall. The reader should note that there exists an alternative way of treating the problem by directly writing Reynolds-averaged turbulent boundary layer equations for the distribution functions  $f_i$  (see Appendix B), which has not been used in this paper.

Let us first define  $\mathbf{x}_1$ ,  $\mathbf{x}_2$  and  $\mathbf{n}$ , respectively the first and second off-wall points and the outward normal unit vector to the wall (see Fig. 2). We also define the density, velocity, deviatoric stress and turbulent viscosity on the boundary node as

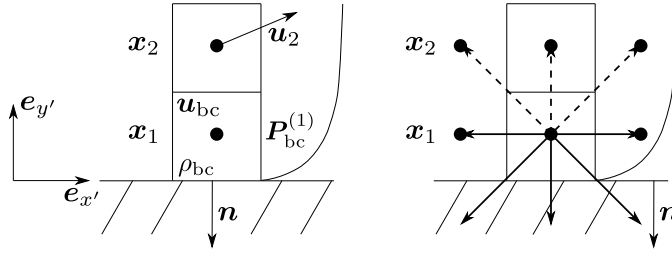


**Fig. 2.** A sketch of the first and second grid points close to the wall. On the left the basic quantities that are computed or imposed for the model. On the right a sketch of the known and missing populations (plain and dashed lines) and the lattice nodes (dots).

$\rho_{bc} \equiv \rho(\mathbf{x}_1)$ ,  $\mathbf{u}_{bc} \equiv \mathbf{u}(\mathbf{x}_1)$ ,  $\hat{\mathbf{P}}_{bc}^{(1)} \equiv \hat{\mathbf{P}}^{(1)}(\mathbf{x}_1)$ , and  $\nu_{t,bc} \equiv \nu_t(\mathbf{x}_1)$ , and the velocity on the second off-wall node as  $\mathbf{u}_2 \equiv \mathbf{u}(\mathbf{x}_2)$ . The proposed algorithm, will impose modifications on the populations and on the relaxation time at position  $\mathbf{x}_1$  according to the reconstruction algorithm of Subsection 2.2, but before going into the details of the modifications, let us first draw the generic concepts used for this boundary condition.

The reconstruction of the populations is based on Eq. (41), where  $\mathbf{u}_{bc}$  (or  $\hat{\mathbf{u}}_{bc}$ ) is given either by a quasi-analytical model such as the Musker law (see Eq. (59)) or by the TBL equation (see Eq. (56)) and  $\rho_{bc}$  and  $\hat{\mathbf{P}}_{bc}^{(1)}$  are given by the procedure described in Subsection 2.2.

Eqs. (59) and (52) are only valid in the frame of reference where the x-axis points in the streamwise direction (let us note this basis component  $\mathbf{e}_{x'}$ ) and the y-axis in the normal to the wall direction pointing inside the domain (let us note this basis component  $\mathbf{e}_{y'} = -\mathbf{n}$ ), and finally the third component of the basis can be chosen as  $\mathbf{e}_{z'} = -\mathbf{e}_{y'} \wedge \mathbf{e}_{x'}$ . All the “primed” quantities are now expressed in this basis (as opposed to the non-primed basis which is the Cartesian one). Let us also define  $\mathbf{R}$  the rotation matrix that relates the primed basis vector with the Cartesian ones

$$\mathbf{e}_{x'} = \mathbf{R}\mathbf{e}_x, \quad \mathbf{e}_{y'} = \mathbf{R}\mathbf{e}_y, \quad \mathbf{e}_{z'} = \mathbf{R}\mathbf{e}_z. \quad (61)$$

Assuming that  $\mathbf{x}_2$  lies within the boundary layer, we will construct the “streamwise” basis vector  $\mathbf{e}_{x'}$  as the  $\mathbf{u}_2$  velocity (computed by LES) to which we removed its projection on the wall’s normal and finally the result is normalized

$$\mathbf{e}_{x'} = \frac{\mathbf{u}_2 - (\mathbf{u}_2 \cdot \mathbf{n})\mathbf{n}}{\|\mathbf{u}_2 - (\mathbf{u}_2 \cdot \mathbf{n})\mathbf{n}\|}. \quad (62)$$

We now want to evaluate  $\mathbf{u}'_{bc}$  which depends on the wall friction  $\tau_w$  (or the velocity wall friction  $u_\tau$ ). In order to determine  $\tau_w$  we will use the fact that  $\mathbf{x}_2$  is assumed to be located in the boundary layer and thus one has that  $u'_2 = \mathbf{u}_2 \cdot \mathbf{e}_{x'}$  follows the boundary layer velocity profile of either Eq. (59) or Eq. (56). With this condition one can solve numerically an implicit equation for the wall friction  $\tau_w$ :

$$u'_2 = \tilde{u}(y_2, \tau_w), \quad (63)$$

where  $y_2 \equiv \mathbf{x}_2 \cdot \mathbf{e}_{y'}$  and  $\tilde{u}(y, \tau_w)$  given by Eq. (59) or (56). In the case of Eq. (59) a simple Newton algorithm is chosen to solve the implicit equation. In the case of Eq. (56) the Newton algorithm must be supplemented by a Gauss–Legendre numerical integration of a 1D partial differential equation.

Once  $\tau_w$  is known, the velocity, velocity gradient, and turbulent viscosity can be explicitly evaluated at  $y_1 \equiv \mathbf{x}_1 \cdot \mathbf{e}_{y'}$ . Therefore one can compute  $u'_{bc} = \tilde{u}(y_1, \tau_w)$  given by Eq. (59) or (56). Then expressing the velocity on the first off-wall cell into the Cartesian frame of reference we obtain

$$\mathbf{u}_{bc} = \mathbf{e}_{x'} u'_{bc}. \quad (64)$$

Computing  $\hat{\mathbf{u}}_{bc}$  thanks to Eq. (36) one can then evaluate  $\rho_{bc}$  by using Eq. (42) and  $\hat{\mathbf{P}}_{bc}^{(1)}$  thanks to Eqs. (45) and (46). With all these quantities one can reconstruct the populations  $\hat{f}_i$  according to Eq. (41). Finally we impose the RANS viscosity of Eq. (57) on  $\mathbf{x}_1$  by applying the following modification to the relaxation frequency which is acting on the viscosity  $\hat{\lambda}_{\nu,bc} \equiv \hat{\lambda}_\nu(y_1) = (\frac{\nu + \nu_{t,bc}}{c_s^2} + \frac{1}{2})^{-1}$  and once the populations on  $\mathbf{x}_1$  have been reconstructed one applies a normal collision-propagation step (see Eqs. (39) and (40)).

#### 4.3. Summary and formulas

In this subsection we quickly explicit the formulas that are used in order to reconstruct the populations  $\hat{f}_i(\mathbf{x}_1)$ , provided that  $\tilde{u}_x$ ,  $\partial_y \tilde{u}_x$  and  $\nu_t$  are known functions.



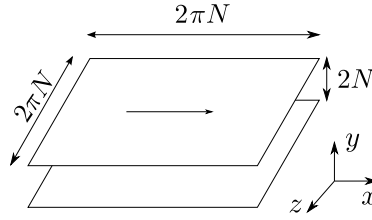


Fig. 3. A sketch of the channel geometry.

1. Compute  $\mathbf{u}_2$  via LES.
2. Determine the basis vector  $\mathbf{e}_{x'}$  thanks to

$$\mathbf{e}_{x'} = \frac{\mathbf{u}_2 - (\mathbf{u}_2 \cdot \mathbf{n})\mathbf{n}}{\|\mathbf{u}_2 - (\mathbf{u}_2 \cdot \mathbf{n})\mathbf{n}\|}.$$

3. Compute  $u_2 = \mathbf{u}_2 \cdot \mathbf{e}_{x'}$ .
4. Compute  $\tau_w$  by solving the implicit equation

$$u'_2 = \tilde{u}(y_2, \tau_w),$$

where  $\tilde{u}(y, \tau_w)$  is given by either Eq. (56) or (59).

5. Compute  $u_1 \equiv u'_{bc}$  thanks to

$$u'_{bc} = \tilde{u}(y_1, \tau_w).$$

6. Compute  $\mathbf{u}_{bc} = u'_{bc} \mathbf{e}_{x'}$  and  $\hat{\mathbf{u}}_{bc} = \hat{\mathbf{u}} - \mathbf{g}/2$ .
7. Compute  $\rho_{bc}$  and  $\hat{\mathbf{p}}_{bc}^{(1)}$  thanks to Eqs. (42) and (46).
8. Compute  $\hat{\lambda}_{v,bc}$  thanks to

$$\hat{\lambda}_{v,bc} = \left( \frac{\nu + \nu_{t,bc}}{c_s^2} + \frac{1}{2} \right)^{-1}.$$

9. Recompute  $\hat{f}_i$  with

$$\hat{f}_i(\mathbf{x}_1) = w_i \rho_{bc} \left( 1 + \frac{\xi_i \cdot \hat{\mathbf{u}}_{bc}}{c_s^2} + \frac{1}{2c_s^4} \mathbf{Q}_i : \hat{\mathbf{u}}_{bc} \hat{\mathbf{u}}_{bc} \right) + \frac{w_i}{2c_s^4} \mathbf{Q}_i : \hat{\mathbf{p}}_{bc}^{(1)}.$$

10. Apply collide-and-stream steps of the LBM algorithm.

## 5. Turbulent plane channel flow simulation

To validate our scheme a turbulent bi-periodic channel has been chosen, because of the high amount of DNS and experimental data available for this test case. Several grid resolutions and Reynolds numbers are considered in order to prevent considering fortuitous error cancellation and misleading conclusions about present model accuracy and robustness [29].

The channel is periodic in the directions  $x$  and  $z$ . Its dimensions are given by  $[2\pi, 2, 2\pi] \times N$ , where  $N$  is the half width of the channel, and the flow is imposed through a body force in the  $x$ -direction (see Fig. 3). The Reynolds number based on the friction velocity and on the average bulk velocity are defined as

$$Re_\tau = \frac{Nu_\tau}{\nu}, \quad (65)$$

$$Re_m = \frac{2Nu_m}{\nu}, \quad (66)$$

where  $u_m = \frac{1}{2} \int_0^2 \langle u_x \rangle dy$  is the mean bulk velocity.

In order to impose the desired mass flow the force is tuned according to the work of Cabrit [7] and is given by

$$\mathbf{g} = u_\tau^2 / N + (u_m - \langle u_x \rangle) \delta t, \quad (67)$$

where  $\delta t = u_m / N$  and  $\langle u_x \rangle$  is the instantaneous space average of the  $x$ -component of the velocity. The target mean bulk velocity is computed by using Dean correlations

$$Re_m = \left( \frac{8}{0.073} \right)^{4/7} Re_\tau^{8/7}. \quad (68)$$

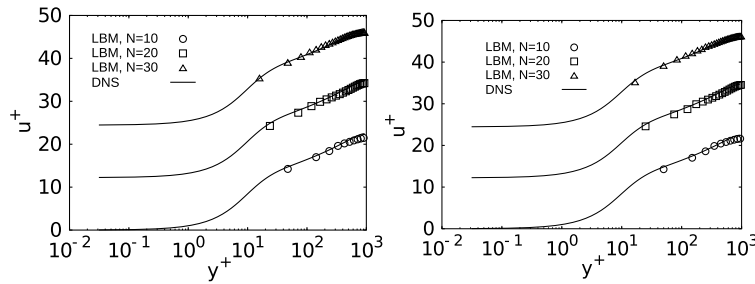


**Fig. 4.** Semi-log plot of  $\bar{u}^+$  with respect to  $y^+$  at  $Re_\tau = 950$  for the Musker profile (left) and the TBL equation (right) with resolution  $N = 10, 20, 30$ . The plain line represents the DNS values of Hoyas and Jiménez, while the LBM computations with  $N = 10$  (circle),  $N = 20$  (square), and  $N = 30$  (triangle).

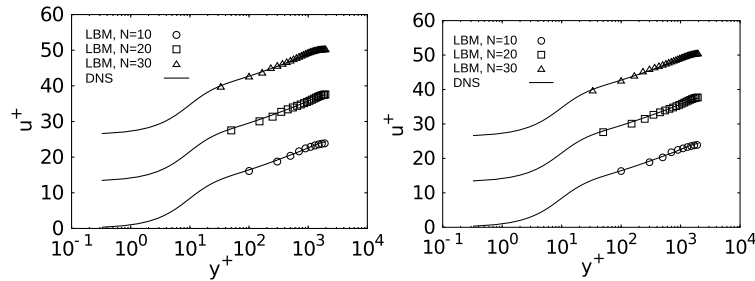


**Fig. 5.** Semi-log plot of  $\bar{u}^+$  with respect to  $y^+$  at  $Re_\tau = 2000$  for the Musker profile (left) and the TBL equation (right) with resolution  $N = 10, 20, 30$ . The plain line represents the DNS values of Hoyas and Jiménez, while the LBM computations with  $N = 10$  (circle),  $N = 20$  (square), and  $N = 30$  (triangle).

For all our simulations we chose  $u_m = 0.1$ . Furthermore all the simulations have been performed for wall laws given by Eqs. (56) and (59).

Simulations are first performed for  $Re_\tau = 950$  and  $2000$ , i.e.  $Re_m = 37042$  and  $86733$  from the Dean correlations, to be able to compare our results with the DNS of Hoyas and Jiménez [19], Hoyas and Jiménez [20]. In each case, three grid resolutions with  $N = 10$ ,  $N = 20$ , and  $N = 30$  are considered, which correspond respectively to 20, 40, and 60 uniformly distributed points within the height of the channel. It is worth noting that uniform grids are used.

For  $Re_\tau = 950$  the first grid point is located at  $y_1^+ = 47.5, 23.75$  and  $15.83$  for  $N = 10, 20$  and  $30$ , respectively. The corresponding mesh size is  $\delta x^+ = \delta y^+ = \delta z^+ = 2y_1^+$ . The Smagorinsky constant was set to  $C = 0.08$ . In the case  $Re_\tau = 2000$  the first grid point is located at  $y_1^+ = 100, 50$  and  $33.33$  (for  $N = 10, 20, 30$ ) and  $C = 0.1$ .

As a comparison wall-resolved LBM-LES has been performed in Premnath et al. [36]. There the simulated Reynolds are of  $Re_\tau = 180, 395$ . Although the simulations are performed on non-uniform grids (and therefore a complete comparison in terms of required computational power is impossible) the resolution needed in the near wall region is of the order of  $\delta y^+ = 1$ . Therefore in the near wall regions the economy in terms of grid points would be of the order of  $10^3$ – $10^5$  for  $Re_\tau = 950$  and of  $10^4$ – $10^6$  for  $Re_\tau = 2000$ .

The computed mean velocity profile  $\bar{u}^+$  is displayed in Figs. 4 and 5 for  $Re_\tau = 950$  and  $Re_\tau = 2000$ , respectively. One can observe a very good agreement between the DNS results and the results obtained with the proposed model. Using the Musker profile or the TBL equation yields almost identical results, as expected in the present channel flow configuration. An interesting point is that the present approach recovers the mean velocity profile and the logarithmic layer in an accurate way, without any kink in the logarithmic law slope. This observation shows that the present approach does not suffer shear-stress-depletion-like problem, even though the wall model is enforced inside the first LES cell only and that no special treatment is applied at the second off-wall cell.

The resolved shear stress profiles  $\bar{u}_x'' u_y''$  are displayed in Figs. 6 and 7. The general accuracy of the results is satisfactory. A kink at the third off-wall grid point is observed, which decreases as the grid resolution is refined. The use of the TBL equation yields slightly better results than the Musker analytical mean velocity profile. This kink does not originate in the specific features of the wall model, but to the use of a classical subgrid viscosity model on a uniform grid with coarse resolution. The rationale for that is that the Smagorinsky model is essentially designed to enforce a correct resolved kinetic energy budget in isotropic turbulence. Therefore, using it on very coarse cubic cells in strongly anisotropic sheared turbulence yields a poor estimate of the sub grid energy transfers, yielding the anisotropic growth of errors on the resolved field. Such a behavior can be minimized for Navier–Stokes computations, since they allow for the use of non-uniform Cartesian grids that are better suited to capture flow physics.

The last test deals with the robustness of the proposed method at very high Reynolds number on very coarse grids such that the full inner layer is encompassed within the first LES cell. To this end, simulations at  $Re_\tau = 20000$  (i.e.  $Re_m = 1.21 \cdot 10^6$ ) are performed considering  $N = 10, 20, 30$ . The first point is located at  $y_1^+ = 1000, 500$  and  $333$  depending on the resolution. The Smagorinsky constant is set equal to  $C = 0.25$ , which is above the usual values used, but which reflects the

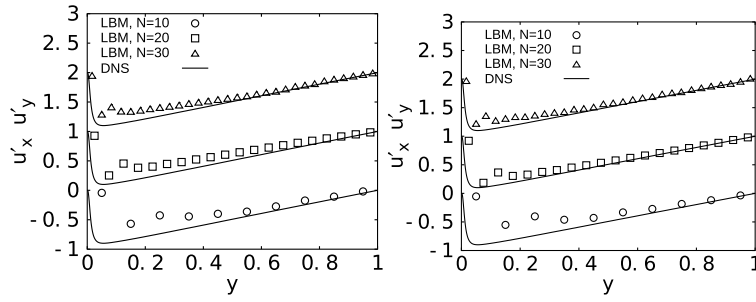


**Fig. 6.** Plot of  $\widetilde{u'_x u'_y}$  with respect to  $y$  at  $Re_\tau = 950$  for the Musker profile (left) and the one dimensional equation (right) with resolution  $N = 10, 20, 30$ . The plain line represents the DNS values of Hoyas and Jiménez, while the LBM computations with  $N = 10$  (circle),  $N = 20$  (square), and  $N = 30$  (triangle).

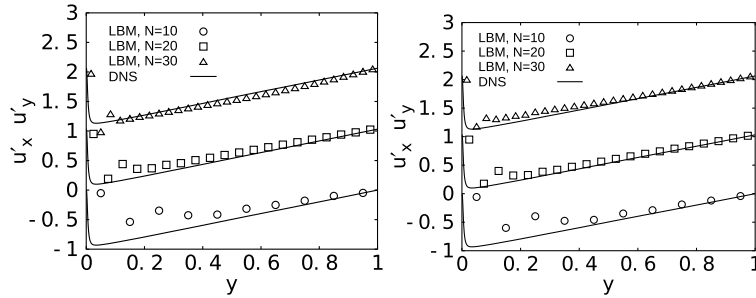


**Fig. 7.** Plot of  $\widetilde{u'_x u'_y}$  with respect to  $y$  at  $Re_\tau = 2000$  for the Musker profile (left) and the one dimensional equation (right) with resolution  $N = 10, 20, 30$ . The plain line represents the DNS values of Hoyas and Jiménez, while the LBM computations with  $N = 10$  (circle),  $N = 20$  (square), and  $N = 30$  (triangle).

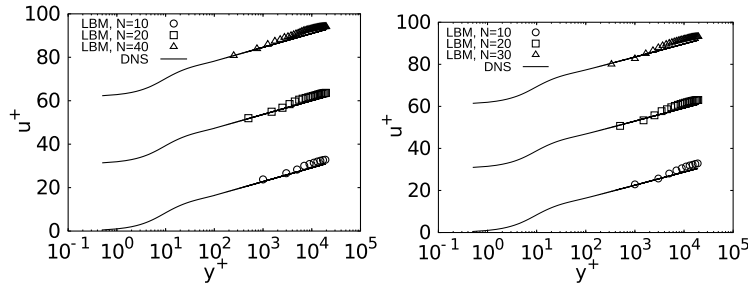


**Fig. 8.** Semi-log plot of  $\bar{u}^+$  with respect to  $y^+$  at  $Re_\tau = 20000$  with resolution  $N = 10, 20, 30$  and the analytical law of Monkewitz et al. [31] (respectively circles, squares, triangles, and plain line).

degree of under resolution of the problem. In this extreme case, the under-resolution with respect to a classical DNS (in terms of grid points) is about  $1000^3$ – $2000^3$ . Since there is no DNS or experimental data available at this Reynolds number, the results are compared with the analytical profile of Musker [32].

The mean velocity profile is displayed in Fig. 8. The quality of the results is good, but a little bit less satisfactory than the one recovered at lower Reynolds number. The computed results do not exactly follow the semi-analytical law of Musker. The reason may be that either the simulation is too severely underresolved, or that the analytical law is not accurate enough because it is too far from the logarithmic region of the boundary layer. But we can see a convergence of the results as the resolution is increased.

In order to provide a more quantitative discussion let us study the error made on the average velocity field for each Reynolds number. The average error is defined as

$$E = \frac{1}{M} \sqrt{\sum_{i=0}^{M-1} \frac{(\bar{u}^+(y_i^+) - \bar{u}_{\text{ref}}^+(y_i^+))^2}{\bar{u}_{\text{ref}}^+(y_i^+)^2}} \cdot 100, \quad (69)$$

where  $\bar{u}^+(y_i^+)$  and  $\bar{u}_{\text{ref}}^+(y_i^+)$  are respectively the LBM velocity and reference (DNS or semi-analytical profile) velocity at point  $y_i^+$ . We display  $E$  for different Reynolds numbers in Table 1. One can see that the results are almost the same for the Musker law and one dimensional equation model. Furthermore they are of roughly the same value for  $Re_\tau = 950$  and  $Re_\tau = 2000$ . The error is increased by a factor of four for  $Re_\tau = 20000$ . For all the cases the error is of order one since it decreases linearly with the resolution.

**Table 1**

The average error on the average velocity profile made for  $Re_\tau = 950, 2000, 20000$  (left, center, right respectively) with respect to the resolution for the Musker law model and one dimensional equation model (center and right column respectively).

$N$	$E_{\text{Musker}}$	$E_{1d}$	$N$	$E_{\text{Musker}}$	$E_{1d}$	$N$	$E_{\text{Musker}}$	$E_{1d}$
10	2.11	2.05	10	2.32	2.05	10	8.31	9.05
20	1.07	1.08	20	1.15	1.10	20	4.07	4.61
30	0.83	0.81	30	0.88	0.88	30	2.92	3.11

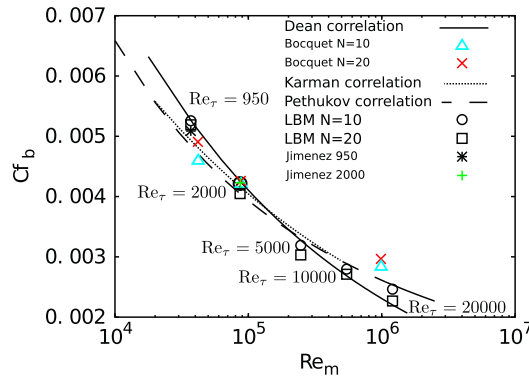


**Fig. 9.** Bulk friction coefficient with respect to the mean Reynolds number. The plain, dotted and dashed lines represent respectively the results of the Dean, Karman–Nikuradse, and Pethukov correlations while the circles and squares are respectively the results for  $N = 10, 20$  and for all the  $Re_\tau$  tested, the crosses and the triangles are the results of Bocquet et al. for  $N = 10, 20$  respectively, and the star and cross are the results of the DNS of Hoyas and Jiménez.

Finally the error on the bulk friction coefficient  $Cf_b$  is plotted versus the bulk Reynolds number, see Fig. 9, with

$$Cf_b = 2/u_m^{+2} = 2u_\tau^2/u_m^2. \quad (70)$$

Present results are compared with predictions given by several semi-empirical formulas and LES results of Bocquet et al. [5]. The error with respect to the Dean correlations for  $Re_m = 950$  ranges from 2.01% to 4.22%. For  $Re_m = 2000$ , the error relative to Dean's law lies between 0.3% and 4.24%. The error level is therefore almost identical for these two Reynolds numbers, and is as good as the one classically reported using Navier–Stokes solvers on similar coarse grids. The error seems to be higher for  $y_1^+ = 50$  at  $Re_m = 950$  and 2000 (respectively  $N = 10$  and  $N = 20$ ). This can be explained by the fact that the Musker profile has an overshoot with respect to the DNS of Hoyas and Jiménez [19,20] at  $y^+ \sim 50$  as noticed in Monkewitz et al. [31]. For  $Re_\tau = 20000$  the error increases to values between 1.11% and 11.8%. The error on the friction coefficient remains below 5% except for very low resolutions, which is a very robust behavior.

As one can see in this particular case, the results obtained with the one-dimensional model and the Musker law are very similar. This similarity is due to the absence of a pressure gradient in the plane channel flow. While the results are very similar the computational power is much bigger when one is using the one-dimensional model since Eq. (56) must be integrated numerically. Depending on the amount of point used in this numerical integration the computational time is increased by a factor of four in the case of about ten integration points, a factor ten with 20 integration points, and factor 200 for 100 integration points.

## 6. Conclusion

In this paper wall-model-LES lattice Boltzmann model was proposed to compute high Reynolds number wall bounded flows. The model was assessed on the turbulent channel flow considering three Reynolds numbers, respectively  $Re_\tau = 1000, 2000$  and 20000, in severely under-resolved situations which allowed an economy in terms of number of grid points by a factor about  $10^6$  and  $10^9$  with respect to a DNS (depending on the Reynolds number), while keeping the average velocity in very good agreement with either a DNS or semi-analytical profiles. The model also exhibits a good Reynolds stress profile prediction and a very good recovery of the friction coefficient.

## Acknowledgements

Orestis Malaspinas and Pierre Sagaut acknowledge the support of FUI via the LaBS project [1]. O. Malaspinas acknowledges the Scylla, Andromeda, and Perseus clusters of the University of Geneva. O. Malaspinas would like to thankfully acknowledge the support of the Swiss National Science Foundation SNF (Award PA00P2\_145364).

## Appendix A. MRT transformation matrix

A possible choice of transformation matrix  $\mathbf{M}$  reads (see d'Humières et al. [13])

$$\mathbf{M} = \begin{pmatrix} 1 & 1 & 1 & 1 & 1 & 1 & 1 & 1 & 1 & 1 & 1 & 1 & 1 & 1 & 1 & 1 & 1 & 1 \\ -30 & -11 & -11 & -11 & 8 & 8 & 8 & 8 & 8 & 8 & -11 & -11 & -11 & 8 & 8 & 8 & 8 & 8 \\ 12 & -4 & -4 & -4 & 1 & 1 & 1 & 1 & 1 & 1 & -4 & -4 & -4 & 1 & 1 & 1 & 1 & 1 \\ 0 & -1 & 0 & 0 & -1 & -1 & -1 & -1 & 0 & 0 & 1 & 0 & 0 & 1 & 1 & 1 & 1 & 0 \\ 0 & 4 & 0 & 0 & -1 & -1 & -1 & -1 & 0 & 0 & -4 & 0 & 0 & 1 & 1 & 1 & 1 & 0 \\ 0 & 0 & -1 & 0 & -1 & 1 & 0 & 0 & -1 & -1 & 0 & 1 & 0 & 1 & -1 & 0 & 0 & 1 \\ 0 & 0 & 4 & 0 & -1 & 1 & 0 & 0 & -1 & -1 & 0 & -4 & 0 & 1 & -1 & 0 & 0 & 1 \\ 0 & 0 & 0 & -1 & 0 & 0 & -1 & 1 & -1 & 1 & 0 & 0 & 1 & 0 & 0 & 1 & -1 & -1 \\ 0 & 0 & 0 & 4 & 0 & 0 & -1 & 1 & -1 & 1 & 0 & 0 & -4 & 0 & 0 & 1 & -1 & 1 \\ 0 & 2 & -1 & -1 & 1 & 1 & 1 & 1 & -2 & -2 & 2 & -1 & -1 & 1 & 1 & 1 & 1 & -2 \\ 0 & -4 & 2 & 2 & 1 & 1 & 1 & 1 & -2 & -2 & -4 & 2 & 2 & 1 & 1 & 1 & 1 & -2 \\ 0 & 0 & 1 & -1 & 1 & 1 & -1 & -1 & 0 & 0 & 0 & 1 & -1 & 1 & 1 & -1 & -1 & 0 \\ 0 & 0 & -2 & 2 & 1 & 1 & -1 & -1 & 0 & 0 & 0 & -2 & 2 & 1 & 1 & -1 & -1 & 0 \\ 0 & 0 & 0 & 0 & 1 & -1 & 0 & 0 & 0 & 0 & 0 & 0 & 0 & 1 & -1 & 0 & 0 & 0 \\ 0 & 0 & 0 & 0 & 0 & 0 & 0 & 0 & 1 & -1 & 0 & 0 & 0 & 0 & 0 & 0 & 0 & 1 \\ 0 & 0 & 0 & 0 & 0 & 0 & 1 & -1 & 0 & 0 & 0 & 0 & 0 & 0 & 0 & 1 & -1 & 0 \\ 0 & 0 & 0 & 0 & -1 & -1 & 1 & 1 & 0 & 0 & 0 & 0 & 0 & 1 & 1 & -1 & -1 & 0 \\ 0 & 0 & 0 & 0 & 1 & -1 & 0 & 0 & -1 & -1 & 0 & 0 & 0 & -1 & 1 & 0 & 0 & 1 \\ 0 & 0 & 0 & 0 & 0 & 0 & -1 & 1 & 1 & -1 & 0 & 0 & 0 & 0 & 0 & 1 & -1 & 1 \end{pmatrix}.$$

The relaxation times which are not determined by the viscosity are given by

$$\lambda_0 = \lambda_3 = \lambda_5 = \lambda_7 = 1,$$

$$\lambda_1 = 1.19, \quad \lambda_2 = \lambda_{10} = \lambda_{12} = 1.4,$$

$$\lambda_4 = \lambda_6 = \lambda_8 = 1.2,$$

$$\lambda_{16} = \lambda_{17} = \lambda_{18} = 1.98.$$

The relaxation times related to the kinematic viscosity  $\nu$  are given by

$$\lambda_\nu \equiv \lambda_9 = \lambda_{11} = \lambda_{13} = \lambda_{14} = \lambda_{15} = \left( \frac{\nu}{c_s^2} + \frac{1}{2} \right)^{-1} \quad (\text{A.1})$$

## Appendix B. Reynolds-averaged turbulent boundary layer equations for the Boltzmann BGK equation

In this appendix we quickly present the TBL equation in the Boltzmann equation framework. For simplicity, our starting point is the continuous Boltzmann with a single relaxation time, or BGK Boltzmann equation (see Bhatnagar et al. [4])

$$\partial_t f_i(\mathbf{x}, t) + \xi_i \cdot \nabla f_i(\mathbf{x}, t) = -\frac{1}{\tau} (f_i(\mathbf{x}, t) - f_i^{(0)}(\mathbf{x}, t)) + F_i. \quad (\text{B.1})$$

In this section, inspired by [26] and the classical Reynolds-averaged Navier–Stokes (RANS) equations theory, we will write the Reynolds-averaged Boltzmann (RAB) equations (different RAB approaches have also been proposed in Orszag et al. [34], Latt et al. [22]).

Taking the average of Eq. (B.1), one can write the Reynolds-averaged BGK equation as

$$\partial_t \langle f_i \rangle + \xi_i \cdot \nabla \langle f_i \rangle = -\frac{1}{\tau} (\langle f_i \rangle - \langle f_i^{(0)}(\rho, \mathbf{u}) \rangle) + \langle F_i \rangle, \quad (\text{B.2})$$

where  $\langle F_i \rangle$  is given by

$$\langle F_i \rangle = w_i \langle \rho \rangle \left( \frac{\xi_i \cdot \tilde{\mathbf{u}}}{c_s^2} - \frac{(\xi_i \cdot \tilde{\mathbf{u}}) \xi_i}{c_s^4} \right) \cdot \tilde{\mathbf{g}}, \quad (\text{B.3})$$

and  $\overline{f_i^{(0)}(\rho, \mathbf{u})}$  can be rewritten as

$$\overline{f_i^{(0)}(\rho, \mathbf{u})} = w_i \langle \rho \rangle \left( 1 + \frac{\xi_i \cdot \tilde{\mathbf{u}}}{c_s^2} + \frac{1}{2c_s^2} \mathbf{Q}_i : \tilde{\mathbf{u}} \tilde{\mathbf{u}} \right) + \frac{1}{2c_s^4} \mathbf{Q}_i : (\langle \rho \rangle \widetilde{\mathbf{u}'' \mathbf{u}''}). \quad (\text{B.4})$$

The Reynolds-averaged Boltzmann equation can therefore be rewritten as

$$\partial_t \langle f_i \rangle + \xi_i \cdot \nabla \langle f_i \rangle = -\frac{1}{\tau} (\langle f_i \rangle - f_i^{(0)}(\langle \rho \rangle, \tilde{\mathbf{u}})) + \frac{\langle \rho \rangle}{2\tau c_s^4} \mathbf{Q}_i : \widetilde{\mathbf{u}'' \mathbf{u}''} + \langle F_i \rangle, \quad (\text{B.5})$$

with  $\langle \rho \rangle \widetilde{\mathbf{u}'' \mathbf{u}''}$  being the Reynolds stress tensor that needs to be modeled.

In our case the Reynolds stresses will be modeled with the help of an eddy viscosity model,

$$\langle \rho \rangle \widetilde{\mathbf{u}'' \mathbf{u}''} = -2\mu_t \tilde{\mathbf{S}}. \quad (\text{B.6})$$

Following Malaspinas and Sagaut [26], one implements such models by including the eddy viscosity in the relaxation time  $\tau$  such that it is replaced by an efficient relaxation time,

$$\tau_{\text{eff}} = \tau + \tau_t, \quad (\text{B.7})$$

where

$$\tau_t = \mu_t / (c_s^2 \langle \rho \rangle). \quad (\text{B.8})$$

Finally the modified Boltzmann-BGK equation to be simulated is given by

$$\partial_t \langle f_i \rangle + \xi_i \cdot \nabla_{\mathbf{x}} \langle f_i \rangle = -\frac{1}{\tau_{\text{eff}}} (\langle f_i \rangle - f_i^{(0)}(\langle \rho \rangle, \tilde{\mathbf{u}})) + \langle F_i \rangle. \quad (\text{B.9})$$

The equations can be further simplified assuming that the flow is parallel and statistically steady. Considering that  $x$  and  $y$  directions are, as in Subsection 4.2, aligned respectively with the streamwise direction and the normal to the wall, the RAB equation can be rewritten as

$$\xi_{ix} \partial_x \langle f_i \rangle + \xi_{iy} \partial_y \langle f_i \rangle = -\frac{1}{\tau} (\langle f_i \rangle - f_i^{(0)}(\langle \rho \rangle, \tilde{\mathbf{u}})) - \frac{\mu_t}{2\tau c_s^4} Q_{ixy} \partial_y \tilde{u}_x + \langle F_i \rangle, \quad (\text{B.10})$$

where  $\tilde{\mathbf{u}}$  and  $\nabla \tilde{\mathbf{u}}$  are prescribed by a RANS velocity profile (see Eqs. (50)–(52) or Eq. (59)). Using Eq. (54) and  $\tilde{g}_y = 0$  (assumption which holds in the turbulent channel flow)  $f_i^{(0)}$  and  $\langle F_i \rangle$  can be rewritten as

$$f_i^{(0)} = w_i \langle \rho \rangle \left( 1 + \frac{\xi_{ix} \tilde{u}_x}{c_s^2} + \frac{1}{2c_s^4} Q_{ixx} \tilde{u}_x^2 \right) \quad (\text{B.11})$$

$$\langle F_i \rangle = w_i \langle \rho \rangle \left( \frac{\xi_{ix} - \tilde{u}_x}{c_s^2} - \frac{(\xi_{ix}^2 \tilde{u}_x)}{c_s^4} \right) \tilde{g}_x. \quad (\text{B.12})$$

We also define a decomposition into an equilibrium and non-equilibrium parts

$$\langle f_i \rangle = f_i^{(0)}(\langle \rho \rangle, \tilde{\mathbf{u}}) + \langle f_i^{\text{neq}} \rangle, \quad (\text{B.13})$$

this time no characteristic magnitude of the non-equilibrium part is assumed (unlike in the Chapman–Enskog expansion, Eq. (21)). Similarly to what is done for  $f_i^{(1)}$ , we define the Favre filtered stress tensor  $\tilde{\mathbf{P}}^{\text{neq}}$  as

$$\tilde{\mathbf{P}}^{\text{neq}} = \sum_i \tilde{\mathbf{c}}_i \tilde{\mathbf{c}}_i \langle f_i^{\text{neq}} \rangle, \quad (\text{B.14})$$

where  $\tilde{\mathbf{c}}_i = \xi_i - \tilde{\mathbf{u}}$ . As for  $f_i^{(1)}$ ,  $\langle f_i^{\text{neq}} \rangle$  possesses the following properties

$$\sum_i \langle f_i^{\text{neq}} \rangle = \sum_i \xi_i \langle f_i^{\text{neq}} \rangle = 0, \quad (\text{B.15})$$

which are consequences of the mass and momentum conservation. Finally we assume that  $\langle f_i \rangle$  is given by a Hermite expansion up to order two, which is the order required in order for the BGK equation to lead to the Navier–Stokes equations (see Subsection 2.1), and thus has the following form

$$\langle f_i \rangle = \underbrace{w_i \langle \rho \rangle \left( 1 + \frac{\xi_i \cdot \tilde{\mathbf{u}}}{c_s^2} + \frac{1}{2c_s^4} \mathbf{Q}_i : \tilde{\mathbf{u}} \tilde{\mathbf{u}} \right)}_{f_i^{(0)}(\langle \rho \rangle, \tilde{\mathbf{u}})} + \underbrace{\frac{w_i}{2c_s^4} \mathbf{Q}_i : \tilde{\mathbf{P}}^{\text{neq}}}_{\langle f_i^{\text{neq}} \rangle}. \quad (\text{B.16})$$

With all these assumptions in mind, one can take the first and second order moment of Eq. (B.10) where we used Eqs. (B.11)–(B.12), along with assumptions of Eq. (54), and find two sets of equations for the components of  $\tilde{\mathbf{P}}^{\text{neq}}$

$$\partial_y \tilde{P}_{xy}^{\text{neq}} = \langle \rho \rangle \tilde{g} - \partial_x \langle p \rangle, \quad (\text{B.17})$$

$$\partial_y \tilde{P}_{yy}^{\text{neq}} = 0, \quad (\text{B.18})$$

$$\partial_y \tilde{P}_{yz}^{\text{neq}} = 0, \quad (\text{B.19})$$

and

$$\tilde{P}_{xx}^{\text{neq}} = 2\mu\tilde{u}_x\tilde{g}_x/c_s^2, \quad (\text{B.20})$$

$$\tilde{P}_{yy}^{\text{neq}} = 0, \quad (\text{B.21})$$

$$\tilde{P}_{zz}^{\text{neq}} = 0, \quad (\text{B.22})$$

$$\tilde{P}_{xy}^{\text{neq}} = -(\mu + \mu_t)\partial_y\tilde{u}_x, \quad (\text{B.23})$$

$$\tilde{P}_{yz}^{\text{neq}} = 0, \quad (\text{B.24})$$

$$\tilde{P}_{xz}^{\text{neq}} = 0. \quad (\text{B.25})$$

Since  $\langle\rho\rangle$ ,  $\tilde{\mathbf{u}}$  and  $\tilde{\mathbf{P}}^{\text{neq}}$  can be computed, the populations can therefore be reconstructed with Eq. (B.16).

## References

- [1] LaBS project, <http://www.labs-project.org>.
- [2] C.K. Aidun, R.J. Clausen, Lattice-Boltzmann method for complex flows, *Annu. Rev. Fluid Mech.* 42 (1) (2010) 439–472, <http://dx.doi.org/10.1146/annurev-fluid-121108-145519>.
- [3] Y. Benarafa, O. Cioni, F. Ducros, P. Sagaut, Temperature wall modelling for large-eddy simulation in a heated turbulent plane channel flow, *Int. J. Heat Mass Transf.* 50 (2007) 4360–4370.
- [4] P.L. Bhatnagar, E.P. Gross, M. Krook, A model for collision processes in gases. I. Small amplitude processes in charged and neutral one-component systems, *Phys. Rev.* 94 (3) (1954) 511–525, <http://dx.doi.org/10.1103/PhysRev.94.511>.
- [5] S. Bocquet, P. Sagaut, J. Jouhaud, A compressible wall model for large-eddy simulation with application to prediction of aerothermal quantities, *Phys. Fluids* 24 (6) (2012) 065103, <http://dx.doi.org/10.1063/1.4729614>.
- [6] M. Bouzidi, M. Firdaouss, P. Lallemand, Momentum transfer of a Boltzmann-lattice fluid with boundaries, *Phys. Fluids* 13 (11) (2001) 3452–3459, <http://dx.doi.org/10.1063/1.1399290>.
- [7] O. Cabrit, Direct simulations for wall modeling of multicomponent reacting compressible turbulent flows, *Phys. Fluids* 21 (2009) 055108.
- [8] D.R. Chapman, Computational aerodynamics development and outlook, *AIAA J.* 17 (1979) 1293–1313.
- [9] S. Chapman, T.G. Cowling, *The Mathematical Theory of Nonuniform Gases*, Cambridge University Press, Cambridge, 1960.
- [10] H. Choi, P. Moin, Grid-point requirements for large eddy simulation: Chapman's estimates revisited, *Phys. Fluids* 24 (2012) 011702, <http://dx.doi.org/10.1063/1.3676783>.
- [11] J.W. Deardorff, A numerical study of three-dimensional turbulent channel flow at large Reynolds numbers, *J. Fluid Mech.* 41 (1970) 453–465.
- [12] D. d'Humières, Generalized lattice Boltzmann equations, in: *Rarefied Gas Dynamics: Theory and Simulations*, vol. 159, Am. Inst. Aeronaut. Astronaut., 1992, pp. 450–458.
- [13] D. d'Humières, I. Ginzburg, M. Krafczyk, P. Lallemand, Li-Shi Luo, Multiple-relaxation-time lattice Boltzmann models in three dimensions, *Philos. Trans. R. Soc. Lond. A* 360 (2002) 437–451.
- [14] Y.-H. Dong, P. Sagaut, S. Marié, Inertial consistent subgrid model for large-eddy simulation based on the lattice Boltzmann method, *Phys. Fluids* 20 (3) (2008) 035104, <http://dx.doi.org/10.1063/1.2842379>.
- [15] E. Garnier, N.A. Adams, P. Sagaut, *Large Eddy Simulation for Compressible Flows*, Springer, Berlin, 2009.
- [16] I. Ginzburg, D. d'Humières, Multireflection boundary conditions for lattice Boltzmann models, *Phys. Rev. E* 68 (6) (2003) 066614, <http://dx.doi.org/10.1103/PhysRevE.68.066614>.
- [17] Z. Guo, C. Zheng, An extrapolation method for boundary conditions in lattice Boltzmann method, *Phys. Fluids* 14 (2002) 2007–2010.
- [18] S. Hou, J. Sterling, S. Chen, G.D. Doolen, A lattice Boltzmann subgrid model for high Reynolds number flows, in: *Fields Inst. Commun.*, vol. 6, 1996, pp. 151–166.
- [19] S. Hoyas, J. Jiménez, Scaling of velocity fluctuations in turbulent channels up to  $Re_\tau = 2000$ , *Phys. Fluids* 18 (2006) 011702.
- [20] S. Hoyas, J. Jiménez, Reynolds number effects on the Reynolds-stress budgets in turbulent channels, *Phys. Fluids* 20 (2008) 101511.
- [21] M. Krafczyk, J. Tölke, L.-S. Luo, Large-eddy simulations with a multiple-relaxation-time LBE model, *Int. J. Mod. Phys. B* 17 (2003) 33–39, <http://dx.doi.org/10.1142/S0217979203017059>.
- [22] J. Latt, B. Chopard, S. Succi, F. Toschi, Numerical analysis of the averaged flow field in a turbulent lattice Boltzmann simulation, *Physica A* (ISSN 0378-4371) 362 (1) (2006) 6–10, <http://dx.doi.org/10.1016/j.physa.2005.09.016>.
- [23] J. Latt, B. Chopard, O. Malaspinas, M. Deville, A. Michler, Straight velocity boundaries in the lattice Boltzmann method, *Phys. Rev. E* 77 (5) (2008) 056703, <http://dx.doi.org/10.1103/PhysRevE.77.056703>.
- [24] O. Malaspinas, Lattice Boltzmann method for the simulation of viscoelastic fluid flows, PhD dissertation, EPFL, Lausanne, Switzerland, 2009.
- [25] O. Malaspinas, P. Sagaut, Advanced large-eddy simulation for lattice Boltzmann methods: the approximate deconvolution model, *Phys. Fluids* 23 (2011) 105103, <http://dx.doi.org/10.1063/1.3650422>.
- [26] O. Malaspinas, P. Sagaut, Consistent subgrid scale modelling for lattice Boltzmann methods, *J. Fluid Mech.* 700 (2012) 514–542, <http://dx.doi.org/10.1017/jfm.2012.155>.
- [27] O. Malaspinas, B. Chopard, J. Latt, General regularized boundary condition for multi-speed lattice Boltzmann models, *Comput. Fluids* 49 (1) (2011) 29–35, <http://dx.doi.org/10.1016/j.compfluid.2011.04.010>.
- [28] S. Marié, D. Ricot, P. Sagaut, Comparison between lattice Boltzmann method and Navier–Stokes high-order schemes for computational aeroacoustics, *J. Comput. Phys.* 228 (2009) 1056–1070, <http://dx.doi.org/10.1016/j.jcp.2008.10.021>.
- [29] J. Meyers, P. Sagaut, Is plane channel flow a friendly case for testing of large-eddy simulation subgrid-scale models?, *Phys. Fluids* 19 (2007) 048105.
- [30] D. Monfort, S. Benhamadouche, P. Sagaut, Meshless approach for wall treatment in large-eddy simulation, *Comput. Methods Appl. Mech. Eng.* 199 (2010) 881–889.
- [31] P.A. Monkewitz, K.A. Chauhan, H.M. Nagib, Self-consistent high-Reynolds-number asymptotics for zero-pressure-gradient turbulent boundary layers, *Phys. Fluids* 19 (11) (2007) 115101, <http://dx.doi.org/10.1063/1.2780196>.
- [32] A.J. Musker, Explicit expression for the smooth wall velocity distribution in a turbulent boundary layer, *AIAA J.* 17 (6) (2007) 655–657, <http://dx.doi.org/10.2514/3.61193>.
- [33] H.M. Nagib, K.A. Chauhan, Variations of von Kármán coefficient in canonical flows, *Phys. Fluids* 20 (2008) 101518.
- [34] S.A. Orszag, H. Chen, S. Succi, J. Latt, B. Chopard, Turbulence effects on kinetic equations, *J. Sci. Comput.* (ISSN 0885-7474) 28 (2–3) (2006) 459–466, <http://dx.doi.org/10.1007/s10915-006-9076-x>.
- [35] U. Piomelli, E. Balaras, Wall-layer models for large-eddy simulations, *Annu. Rev. Fluid Mech.* 34 (2002) 349–374.
- [36] Kannan N. Premnath, Martin J. Pattison, Sanjoy Banerjee, Generalized lattice Boltzmann equation with forcing term for computation of wall-bounded turbulent flows, *Phys. Rev. E* 79 (2009) 026703, <http://dx.doi.org/10.1103/PhysRevE.79.026703>.

- [37] D. Ricot, S. Marié, P. Sagaut, C. Bailly, Lattice Boltzmann method with selective viscosity filter, *J. Comput. Phys.* (ISSN 0021-9991) 228 (12) (2009) 4478–4490, <http://dx.doi.org/10.1016/j.jcp.2009.03.030>.
- [38] P. Sagaut, *Large Eddy Simulation for Incompressible Flows: An Introduction*, 3rd ed., Springer, Berlin, 2006.
- [39] P. Sagaut, Toward advanced subgrid models for lattice-Boltzmann-based large-eddy simulation: theoretical formulations, *Comput. Math. Appl.* (ISSN 0898-1221) 59 (7) (2010) 2194–2199, <http://dx.doi.org/10.1016/j.camwa.2009.08.051>.
- [40] P. Sagaut, S. Deck, M. Terracol, *Multiscale and Multiresolution Approaches in Turbulence*, 2nd ed., Imperial College Press, London, 2013.
- [41] H. Schlichting, K. Gersten, *Boundary-Layer Theory*, Springer, Berlin, 2000.
- [42] X. Shan, X.-F. Yuan, H. Chen, Kinetic theory representation of hydrodynamics: a way beyond the Navier–Stokes equation, *J. Fluid Mech.* 550 (2006) 413–441, <http://dx.doi.org/10.1017/S0022112005008153>.
- [43] J. Smagorinsky, General circulation experiments with the primitive equations: I. The basic equations, *Mon. Weather Rev.* 91 (1963) 99–164.
- [44] P.R. Spalart, Detached-eddy simulation, *Annu. Rev. Fluid Mech.* 41 (2009) 181–202, <http://dx.doi.org/10.1146/annurev.fluid.010908.165130>.
- [45] S. Succi, *The Lattice Boltzmann Equation for Fluid Dynamics and Beyond*, Oxford University Press, Oxford, 2001.
- [46] H. Xu, P. Sagaut, Optimal low-dispersion low-dissipation LBM schemes for computational aeroacoustics, *J. Comput. Phys.* 230 (13) (2011) 5353–5382, <http://dx.doi.org/10.1016/j.jcp.2011.03.040>.
- [47] H. Xu, O. Malaspinas, P. Sagaut, Sensitivity analysis and determination of free relaxation parameters for the weakly-compressible MRT-LBM schemes, *J. Comput. Phys.* 231 (2012) 7335–7367, <http://dx.doi.org/10.1016/j.jcp.2012.07.005>.
- [48] Q. Zou, X. He, On pressure and velocity boundary conditions for the lattice Boltzmann BGK model, *Phys. Fluids* 9 (1997) 1592–1598.
- [49] P. Quéméré, P. Sagaut, Zonal multi-domain RANS/LES simulations of turbulent flows, *Int. J. Numer. Methods Fluids* 40 (2002) 903–925.
- [50] E. Labourasse, P. Sagaut, Advance in RANS–LES coupling: a review and an insight on the NLDE approach, *Arch. Comput. Methods Eng.* 11 (2004) 199–256.
- [51] E. Balaras, C. Benocci, U. Piomelli, Two-layer approximate boundary conditions for large-eddy simulations, *AIAA J.* 34 (1996) 1111–1119.
- [52] M. Wang, P. Moin, Dynamic wall modeling for large-eddy simulation of complex turbulent flows, *Phys. Fluids* 14 (2002) 2043–2051.
- [53] Y. Benarafa, O. Cioni, F. Ducros, P. Sagaut, TRANS/LES coupling for unsteady turbulent flow simulation at high Reynolds number on coarse meshes, *Comput. Methods Appl. Mech. Eng.* 195 (2006) 2939–2960.
- [54] W. Cabot, P. Moin, Approximate wall boundary conditions in the large-eddy simulation of high Reynolds number flow, *Flow Turbul. Combust.* 63 (1999) 269–291.